# Capillary adsorption of droplets into a funnel-like structure

Yanchen Wu ⓘ,* Fei Wang,† and Weidong Huang
*Institute for Applied Materials–Microstructure Modelling and Simulation (IAM-MMS),*
*Karlsruhe Institute of Technology (KIT), Straße am Forum 7, Karlsruhe 76131, Germany*

Michael Selzer and Britta Nestler
*Institute for Applied Materials–Microstructure Modelling and Simulation (IAM-MMS),*
*Karlsruhe Institute of Technology (KIT), Straße am Forum 7, Karlsruhe 76131, Germany*
*and Institute of Digital Materials Science, Karlsruhe University of Applied Sciences, Moltkestraße 30,*
*Karlsruhe 76133, Germany*

Penetration of liquid with distinct volumes into a funnel-like pore structure is widely observed in nature and technical applications. However, when the droplet size is comparable with the pore size, the penetration criterion, i.e., under which condition the droplet can penetrate into the pore, remains an open question. In this work, we present theoretical models to address the penetration criteria in terms of the droplet size, the intrinsic wettability, and the opening angle of the funnel-shaped structure. The proposed theoretical models are well corroborated by phase-field simulations. Our findings demonstrate a critical contact angle below which a finite-volume droplet can penetrate into a hydrophobic pore. This critical contact angle is intimately related to the opening angle and the droplet size, which provides a complement to previous literature. Note that for a certain-sized droplet, the critical contact angle becomes invariant when the opening angle is greater than a certain threshold. Moreover, we find that for a constant opening angle, the critical contact angle decreases with the increase of the droplet size. As the droplet volume tends to be infinite, the opening angle has almost no influence on the penetration, and the critical contact angle asymptotically approaches $90°$, being consistent with previous works. Our observations illuminate a special mechanism for a precise maneuver of droplets in pore structures with potential applications in filter systems and microfluidic platforms.

## I. INTRODUCTION

The penetration of liquid into a capillary tube has been studied for more than a century [1,2]. The pioneering works of Lucas [3] and Washburn [4] considered the penetration of liquid from an infinite reservoir into a capillary tube, establishing the famous Lucas-Washburn equation. One common conclusion in the previous works is that liquid cannot spontaneously penetrate into a hydrophobic capillary tube with an intrinsic contact angle greater than $90°$. In contrast to previous consideration of infinite-volume liquid, the penetration of a finite-volume droplet into a pore structure is more appealing for practical applications, such as ink-jet printing, coating, and spray cooling [5]. As demonstrated by Marmur [6], when the droplet diameter is comparable with the characteristic length of the capillary tube, a complete penetration of the droplet can be achieved in a capillary tube

---

*yanchen.wu@kit.edu
†fei.wang@kit.edu

with intrinsic contact angles up to 114°. Willmott *et al.* [7] have also shown experimentally that a finite-volume droplet can penetrate into a capillary tube with static contact angles greater than 90°. Indeed, the size effect results from the Laplace pressure induced by the droplet curvature. However, it is still a knotty issue to address the penetration criterion of a finite-volume droplet into a capillary tube as a function of the intrinsic wettability, which shall be discussed in this work.

Apart from the droplet size, the opening angle $2\varphi$ of the pore plays an important role as well. Previous studies about droplet penetration into capillaries focused on straight tubes ($\varphi = 90°$) [7–9], wedge geometries [10–13], cones [14], and others [1]. These geometries may deviate from the pore shape in reality with different opening angles [15,16]. Some other researchers have investigated the influence of pore geometries such as liquid diodes and passive microfluidic valves [17–19] on the liquid movements, but the majority of these works considered infinite-volume droplets. Suffice to say, the mechanisms controlling the penetration behavior of a certain-sized droplet in geometrically confined capillaries have not been completely identified yet. A comprehensive understanding of droplet penetration into geometrically confined capillaries is of crucial significance for a further investigation of the novel biocapillary problems and the development of functional materials with directional water transport properties, to name a few [20–22].

In this work, we consider micrometer-scale droplets penetrating into a funnel-like capillary tube in a quasiequilibrium way. The penetration process is considered as an interplay between the capillary force and the Laplace pressure induced by the droplet curvature to minimize the total free energy. Thus, the penetration behavior can be manipulated by altering the substrate wettability, the opening angle, and the droplet volume. Specifically, we are concerned with limiting configurations for droplets in different sizes penetrating into a pore structure with varying contact angles and opening angles.

In our study, we propose analytical models to address the droplet penetration behavior, and we obtain regime maps of penetration and no penetration. Phase-field simulations are carried out to confirm the theoretical predictions.

## II. PHASE-FIELD METHOD

We apply a volume-preserved Allen-Cahn-type phase-field (PF) model [23] to simulate the droplet penetration behavior. In this model, we introduce a space- and time-dependent variable $\phi(\mathbf{x}, t)$ to characterize the phase state. In particular, the states $\phi(\mathbf{x}, t) = 1$ and 0 stand for the pure liquid and gas phase, respectively. Inside the liquid-gas interface, the variable $\phi(\mathbf{x}, t)$ varies between 0 and 1. The free-energy functional of the system reads [24–28]

$$\mathcal{F} = \int_{\Omega} [(1/\epsilon)w(\phi) + f_0(\phi) + \epsilon\gamma_{lg}(\nabla\phi)^2]d\Omega + \int_{S} f_w(\phi)dS, \tag{1}$$

where $\Omega$ is the spatial domain occupied by the system, $\epsilon$ is related to the width of the liquid-gas interface, and $S$ represents the substrate in contact with the liquid phases. The obstacle potential $w(\phi)$ is formulated as $w(\phi) = (16/\pi^2)\gamma_{lg}\phi(1 - \phi)$ if $0 \leqslant \phi \leqslant 1$, and $w(\phi) = +\infty$ if $\phi < 0$ or $\phi > 1$. The bulk free-energy density $f_0(\phi)$ ensures the volume preservation [23], and $\epsilon\gamma_{lg}(\nabla\phi)^2$ denotes a gradient energy density. In the last term, $f_w$ is the wall free energy density, which is formulated as [25]

$$f_w(\phi) = \gamma_{ls}h(\phi) + \gamma_{gs}[1 - h(\phi)]. \tag{2}$$

Here, $h(\phi) = \phi^3(6\phi^2 - 15\phi + 10)$ depicts an interpolation function, so that $f_w(1) = \gamma_{ls}$ and $f_w(0) = \gamma_{gs}$, where $\gamma_{ls}$ and $\gamma_{gs}$ are, respectively, the surface tensions of the liquid-solid and gas-solid interfaces. By minimizing the free-energy functional based on the variational approach, we obtain the following equation:

$$\tau\epsilon\partial_t\phi = -(16/\pi^2)\gamma_{lg}(1 - 2\phi)/\epsilon + 2\epsilon\gamma_{lg}\Delta\phi - f_0'(\phi), \tag{3}$$
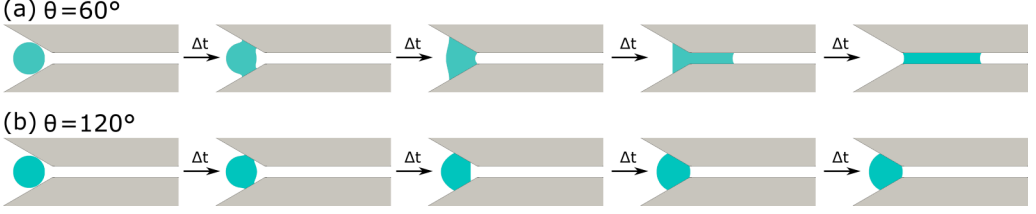
FIG. 1. Droplet evolution with time in a funnel-like structure for different contact angles $\theta$. (a) $\theta = 60°$, (b) $\theta = 120°$. The opening angle of the left wedge is $2\varphi = 60°$. The ratio of the droplet diameter to the channel size is $D/L = 3$.

where $\tau$ is a time relaxation coefficient. The free-energy minimization at the fluid-substrate boundary leads to the following natural boundary condition [28,29]:

$$2\epsilon \gamma_{lg} \nabla \phi \cdot \mathbf{n} + f'_w(\phi) = 0. \tag{4}$$

Here, $\mathbf{n}$ is the normal vector of the solid-liquid boundary. From Eqs. (2) and (4), we obtain

$$2\epsilon \gamma_{lg} \nabla \phi \cdot \mathbf{n} = (\gamma_{gs} - \gamma_{ls}) h'(\phi), \tag{5}$$

which is consistent with Young's law, $\cos \theta = (\gamma_{gs} - \gamma_{ls})/\gamma_{lg}$ [30]. The parameters $\gamma_{lg}$, $\gamma_{ls}$, and $\gamma_{gs}$ determine the contact angle $\theta$.

It should be noted that for a superhydrophobic surface, the order parameter on the substrate beneath the droplet may be smaller than 1. We use the parameters $\phi_{s0}$ and $\phi_{s1}$ to denote the order parameters on the substrate beneath and outside of the droplet, respectively. When the compositions from the substrate to the bulk of liquids are nonuniform, the surface tensions of the liquid-solid and gas-solid interfaces are modified as (see also Refs. [31–33])

$$\gamma_{gs}^* = f_w(\phi_{s0}) + \int_0^{\phi_{s0}} 2\sqrt{\gamma_{lg} w(\phi)} d\phi, \tag{6}$$

$$\gamma_{ls}^* = f_w(\phi_{s1}) + \int_{\phi_{s1}}^1 2\sqrt{\gamma_{lg} w(\phi)} d\phi. \tag{7}$$

The surface compositions on the substrate $\phi_{s0}$ and $\phi_{s1}$ are obtained by solving the equation $2\sqrt{\gamma_{lg} w(\phi)} = f'_w(\phi)$. When the substrate is relatively hydrophobic, we obtain $\phi_{s0} = 0$ and $\phi_{s1} < 1$. In this case, the contact angle is calculated via $\cos \theta = (\gamma_{gs}^* - \gamma_{ls}^*)/\gamma_{lg} = [(\gamma_{gs} - \gamma_{ls}) h(\phi_{s1}) - \int_{\phi_{s1}}^1 2\sqrt{\gamma_{lg} w(\phi)} d\phi]/\gamma_{lg}$. In the next section and Appendix A, we present the validation of the wetting boundary condition and the setups of contact angles in detail.

In the numerical model, variables are nondimensionalized by the characteristic length $x^* = 1 \times 10^{-6}$ m, time $t^* = 1 \times 10^{-9}$ s, and energy $E^* = 1 \times 10^{-11}$ J, respectively. We choose the modeling parameters $\tau = 1$, $\epsilon = 1$, and $\gamma_{lg} = 1$ in the simulations. This model has already been validated for the wetting phenomenon on homogeneous as well as chemically patterned substrates [25,34,35]. Here, we utilize the phase-field model to simulate the droplet penetration into a funnel-like pore structure, which is not only observed in nature but is also used in many technical applications [36–38]. The funnel-shaped structure consists of two parts: the left wedge with an opening angle of $2\varphi$, and the right channel with an inner diameter of $L$. As shown in Fig. 1, a circled droplet with the initial diameter $D$ is initially released inside the left wedge. The inner wall of the wedge is tangential to the droplet profile. Note that we focus mainly on the situation of $D/L > 1$. Driven by the capillary force, the droplet spreads along the inner wall and reaches an equilibrium state eventually. It is observed that the droplet in (a) with a hydrophilic substrate ($\theta = 60°$) completely penetrates into the right channel. However, the droplet in (b) with a hydrophobic ($\theta = 120°$) substrate shows no complete penetration. This reveals that the wettability plays an important role in the penetration. In
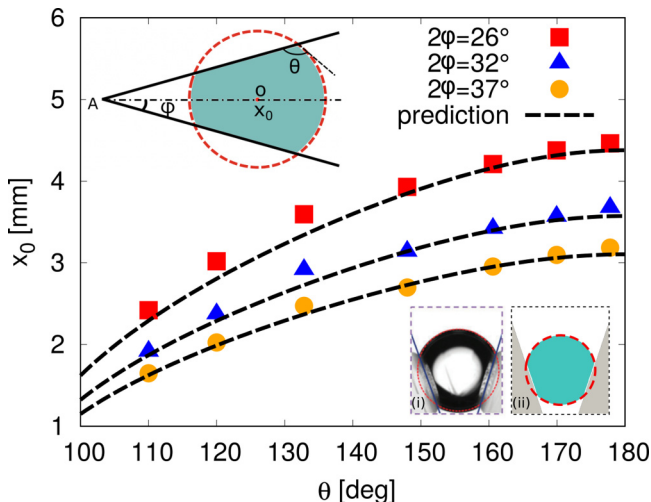
FIG. 2. Validation of the phase-field method for modeling equilibrium states of droplets in a 2D wedge. The distance $x_0$ of the droplet center $O$ from the wedge apex $A$ as a function of the contact angle $\theta$. The colored symbols show the simulation results for droplets with a diameter of $D = 1.96$ mm (the same diameter as the $4 \mu L$-droplet in the experiments of Ref. [12]) in three wedges with opening angles $2\varphi$ ranging from $26°$ to $37°$ and contact angle $\theta$ changing from $110°$ to $180°$. The black dashed lines represent theoretical predictions in two dimensions [see Eq. (8)]. The inset in the top left corner schematically illustrates the equilibrated state of a droplet in a wedge. The insets in the bottom right corner show the equilibrium droplet morphologies for opening angles $2\varphi = 37°$ and contact angle $\theta = 162°$. (i) Experimental results reproduced with permission from Ref. [12]. Copyright 2015 Royal Society of Chemistry; (ii) present 2D phase-field simulation results. The red dashed line is a circular fit of the droplet interface.

the following, we will address the penetration criterion in the funnel-like structure in terms of the wettability, the opening angle, and the droplet size.

## III. VALIDATION OF PHASE-FIELD MODEL

Here, we validate the phase-field model by simulating the equilibrium states of droplets in a wedge in two dimensions. According to Baratian *et al.* [12], the droplet in a wedge at equilibrium is a truncated sphere, as confirmed by the experimental snapshot (i) in Fig. 2. Based on the conclusion of Baratian *et al.* [12], the two-dimensional (2D) droplet in a wedge at equilibrium should be a truncated circle. We simulate the equilibrium droplet shapes in wedges by varying the opening angle and the contact angle. The opening angle $2\varphi$ varies from $26°$ to $37°$ and the contact angle $\theta$ changes from $110°$ to $180°$ (see more details for the setup of the contact angles in Appendix A). The droplet diameter is the same as the one in the paper of Baratian *et al.* [12]. Initially, we release a 2D circled droplet inside the wedge and the droplet evolves to the equilibrium state via surface energy minimization. In Fig. 2, we plot the distance $x_0$ of the droplet center from the wedge apex as a function of the intrinsic Young's contact angle $\theta$. The colored symbols indicate the simulation results for different setups of $(\theta, 2\varphi)$. The dashed lines present the theoretical prediction based on the assumption that the equilibrated droplet is a part of a circle, which is formulated as

$$2x_0/D = \sqrt{\frac{\pi}{-\pi + 2\theta - \sin 2\theta}} \frac{\cos(\pi - \theta)}{\sin \varphi}. \tag{8}$$

Since the drop distance from the apex is larger than the droplet radius, the above equation has to meet with the condition $2x_0/D \geqslant 1$. The insets in the bottom right corner show the equilibrium droplet morphologies for opening angles $2\varphi = 37°$ and contact angle $\theta = 162°$. The snapshots (i) and (ii)
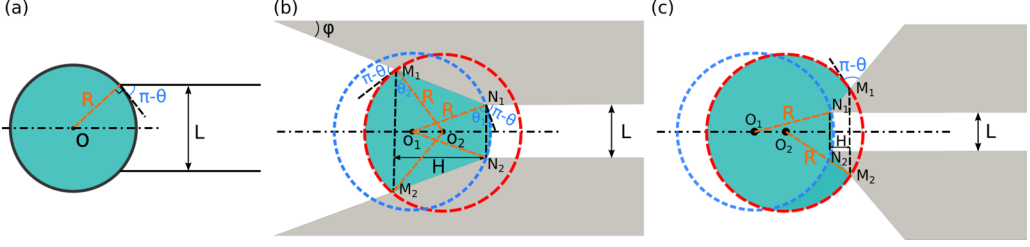
FIG. 3. Schematic of critical states that the droplet cannot completely penetrate into the channel of a funnel-like structure. The dot-dashed line is parallel to the channel wall and passes through the point $O$ (or $O_1$ and $O_2$). $\theta$ represents the static contact angle of the droplet on the substrate and the diameter of the channel is $L$. (a) The droplet has a point contact with the substrate. In (b) and (c), the wedge of the pore has an opening angle of $2\varphi$. The green area indicates the critical state of the droplet. The red and blue dashed circles with radii $R$ fit the left and right droplet interfaces, respectively. $M_1$, $M_2$, $N_1$, and $N_2$ are contact points of the three phases. (b) $\varphi \in (0, \pi/2]$. $\theta_1 = \angle O_1 N_1 N_2$, $\theta_2 = \angle O_2 M_1 M_2$. (c) $\varphi \in (\pi/2, \pi)$.

indicate the experimental result from Ref. [12] and the present 2D simulation result, respectively. The droplet shapes show a great agreement with the dashed circular fits. The good consistency of the simulation results with the experiments and theoretical predictions reveals the capability of the numerical model to simulate the wetting behavior in a confined geometry.

## IV. ANALYTICAL MODEL

In this section, we propose two theoretical models to address the penetration criterion of a droplet into the channel of the funnel-like structure, as illustrated in Fig. 3. We consider a droplet with an initial diameter of $D$. When the contact angle $\theta \leqslant 90°$, the droplet can always penetrate into the funnel-like structure, as studied in many references [11,13,39,40]. Hence, we focus here on the situation in which the contact angle is greater than $90°$.

Model 1 is described in Fig. 3(a), which shows a special penetration critical state in which the droplet cannot penetrate into the channel. In this case, the droplet is a complete circle in two dimensions (2D) and has a point contact with the substrate. In three dimensions (3D), it is a sphere and has a line contact with the substrate (cylinder tube). To fulfill the wetting boundary condition in the channel, we have the expression for calculating the radius of the droplet in the channel: $R = 0.5L/\cos(\pi - \theta)$, which is also equal to the initial radius of the droplet. Thus this critical state can be described by the following equation both in 2D and 3D (model 1):

$$\frac{D}{L} = -\frac{1}{\cos\theta}. \tag{9}$$

For a certain droplet size $D/L$, solving Eq. (9) for $\theta$ yields the critical contact angle $\theta_c$ above which penetration occurs. The curve described by Eq. (9) is called the penetration critical line. Thus we obtain the penetration criterion: when $\theta < \theta_c$, penetration occurs; when $\theta > \theta_c$, no penetration takes place. Note that $\varphi$ does not appear in model 1. The details for the validity of model 1 [Eq. (9)] will be discussed in the following.

In general cases, the left and the right interfaces of the equilibrium 2D droplet may not be on a joint circle. This fact is considered in model 2, as presented in Figs. 3(b) ($0 < \varphi \leqslant \pi/2$) and 3(c) ($\pi/2 < \varphi < \pi$). Here, the blue and red dashed circles depict the left and right interfaces of the 2D droplet, respectively. At equilibrium, these two circles have the same curvature radius $R$ to be consistent with the uniform Young-Laplace pressure inside the droplet. We refer to this state as the (penetration) critical state for the droplet. Fulfilling the wetting boundary conditions and the volume

conservation, we obtain the penetration critical state described by model 2 in 2D:

$$\frac{D}{L} = \sqrt{\frac{2(\theta - \pi) + \alpha + \sin\alpha + \sin 2\theta + \cot\varphi(\cos\alpha - \cos 2\theta)}{2\pi\cos^2\theta}}, \tag{10}$$

where $\alpha = 2\theta + 2\varphi$.

The 3D structures are obtained by rotating the 2D geometries along the dot-dashed center lines. In this case, model 2 in 3D becomes

$$\frac{D}{L} = \frac{\sqrt[3]{0.25[\cot\varphi(\cos^3\theta_2 - \cos^3\theta_1) + \sum_{i=1}^{2}(2 + \sin\theta_i)(1 - \sin\theta_i)^2]}}{\cos\theta_1}, \tag{11}$$

with the angles $\theta_1 = \pi - \theta$ and $\theta_2 = \pi - \theta - \varphi$. For certain values of $D/L$ and $\varphi$, solving Eqs. (10) or (11) for $\theta$ gives rise to the critical contact angle $\theta_c$ above which penetration occurs. The curve described by Eqs. (10) or (11) is called the penetration critical line. Thus we have the penetration criterion: when $\theta < \theta_c$, penetration occurs; when $\theta > \theta_c$, no penetration takes place. See the Appendixes B and C for calculation details of model 2 in 2D and 3D, respectively.

Note that there is a special case for model 2 where the red and blue dashed circles in Figs. 3(b) and 3(c) overlap with each other, which is equivalent to a boundary state,

$$\varphi_t/2 + \theta_t = \pi. \tag{12}$$

Here, $2\varphi_t$ and $\theta_t$ denote the opening angle and the contact angle for the boundary state, respectively. This special state corresponds to the situation in which the equilibrium droplet has a point (in 2D) or line contact (in 3D) with the throat, and its contact angles on the wall of the left wedge and the inner wall of the channel are the same, i.e., $\theta = \theta_t = \pi - \varphi_t/2$. Substituting Eq. (12) into Eqs. (10) or (11), we obtain the same criterion as model 1. Actually, when $\varphi \geqslant \varphi_t = 2\pi - 2\theta_t$, the opening angle does not affect the penetration behavior anymore. In this case, the critical state of the droplet penetration is depicted by model 1. Thus models 1 and 2 are valid for $\varphi \geqslant \varphi_t$ and $0 < \varphi \leqslant \varphi_t$, respectively.

## V. RESULTS AND DISCUSSIONS

In this section, we investigate numerically and analytically the influence of the opening angle $2\varphi$, the contact angle $\theta$, and the droplet size $D/L$ on the droplet penetration behavior. In the numerical simulation, a droplet is initially released on the left side of the wedge, contacting the substrate. For different opening angles and contact angles, we achieve distinct equilibrium states of the droplet. Exemplary 2D simulation results are illustrated in Fig. 4(a) for $D/L = 3$. In Fig. 4(b), we plot the penetration states from the 2D simulations in the ranges $\varphi \in [10°, 150°]$ and $\theta \in [80°, 140°]$. The squares and triangles indicate the states of penetration and no penetration into the channel of the pore structure, respectively. The theoretical prediction via model 1 ($\varphi \in [140°, 150°]$) and model 2 in 2D ($\varphi \in [10°, 140°]$) is depicted by the solid line, which is very consistent with the simulation results in the studied range. It is further observed that for a fixed opening angle, a large contact angle tends to prevent the penetration, and that for a fixed contact angle in the range of $\theta \in (96°, 110°)$, a large opening angle facilitates the penetration.

Figure 4(c) presents the effect of the droplet size $D/L$ on the penetration critical lines, where different droplet sizes $D/L$ correspond to distinct colored solid lines. The theoretically predicted penetration critical lines are obtained by solving Eqs. (9) and (10) for different values of $D/L$. The colored circle points indicate the 2D simulation results, where the scattering bar is a result of the binary search algorithm. For instance, we initially run two simulations with contact angles $\theta_I$ and $\theta_{II}$. The selection for the contact angles is guided by the theoretical value $\theta_c$, such that $\theta_I < \theta_c < \theta_{II}$, and it leads to penetration and no penetration states, respectively, for $\theta_I$ and $\theta_{II}$. The so-called binary search algorithm compares these two simulation results to the one for $\theta_m := (\theta_I + \theta_{II})/2$. If penetration takes place for $\theta_m$, we replace $\theta_I$ by $\theta_m$; otherwise, $\theta_{II}$ is replaced by $\theta_m$. We repeat
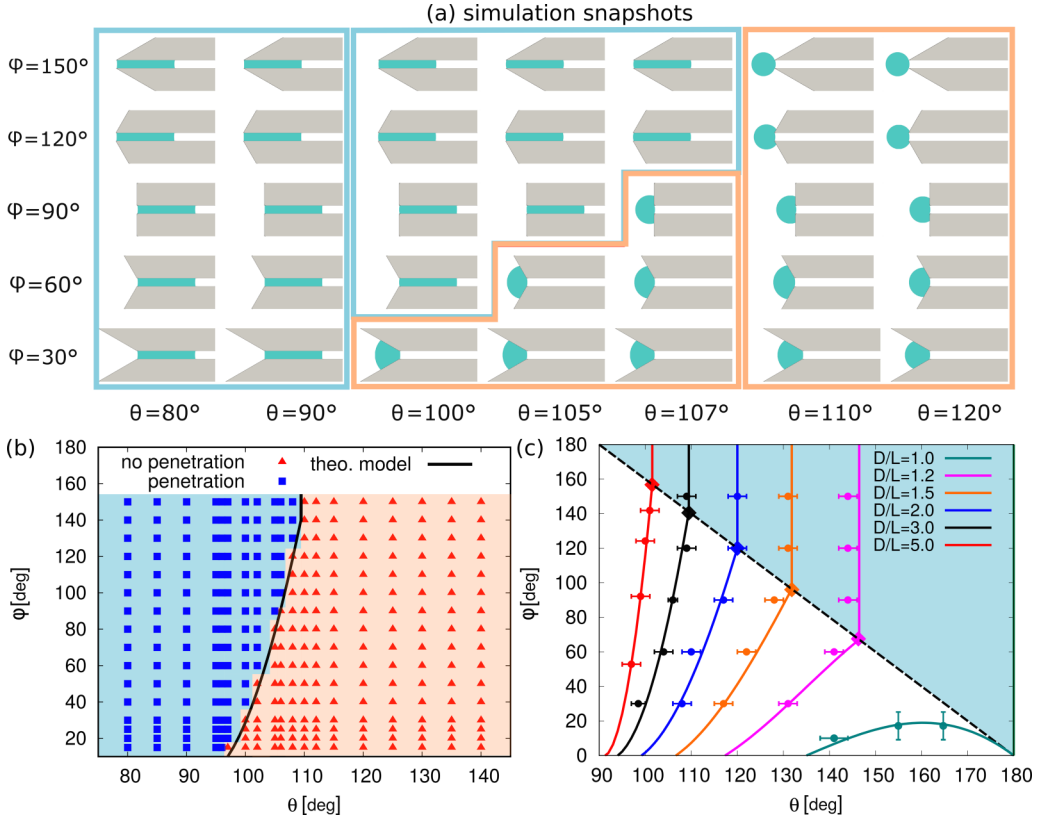
FIG. 4. Penetration criterion diagrams in funnel-like pore structures as a function of $\varphi$ and $\theta$. (a) Final states of droplets ($D/L = 3$) with varying $\varphi$ and $\theta$. (b) Regime diagram for the penetration states of the droplet with $D/L = 3$. Blue squares, complete penetration into the channel of the pore structure; red triangles, no penetration. The penetration critical line via the theoretical model is indicated by the solid line. (c) The penetration critical lines predicted from the theoretical model for different $D/L$. The colored rhombus points are intersections of models 1 and 2. The black dashed line passing through these rhombus points is described by Eq. (12). The circle points with scattering bars via the binary search algorithm indicate the simulation results for the critical state.

this procedure successively for the new $\theta_{\mathrm{I}}$ and $\theta_{\mathrm{II}}$ until the critical state is found within a relatively narrow interval. At the end of the binary search procedure, the critical state from the simulation is represented by $\theta_m$ and the scattering bar is obtained according to the difference of the final $\theta_{\mathrm{I}}$ and $\theta_{\mathrm{II}}$. The intersections ($\theta_t$, $\varphi_t$) between model 1 (straight part of the solid lines) and model 2 in 2D (curved part of the solid lines) are illustrated with the rhombus points. The black dashed line passing through these intersections corresponds to Eq. (12), which divides the whole region into two zones, namely the blue zone ($\varphi \geqslant \varphi_t$) and the white zone [$\varphi \in (0°, \varphi_t)$]. The simulation results coincide excellently with model 1 in the blue zone as well as with model 2 in the white zone. This implies that the equilibrated droplet in the blue zone has only a point contact with the substrate. A typical result for the scenario of a point contact inside the blue zone is demonstrated in Fig. 4(a) for the setup ($\theta = 120°$, $\varphi = 150°$).

For a certain-sized droplet, the critical contact angle increases with the opening angle until a certain value $\varphi_t$ is achieved. Above $\varphi_t$, the critical contact angle is a constant value. The value of $\varphi_t$ increases with the droplet size $D/L$, implying that the penetration behavior of a larger droplet can be manipulated by adjusting the opening angle in a wider range [$\varphi \in (0°, \varphi_t)$]. Moreover, the
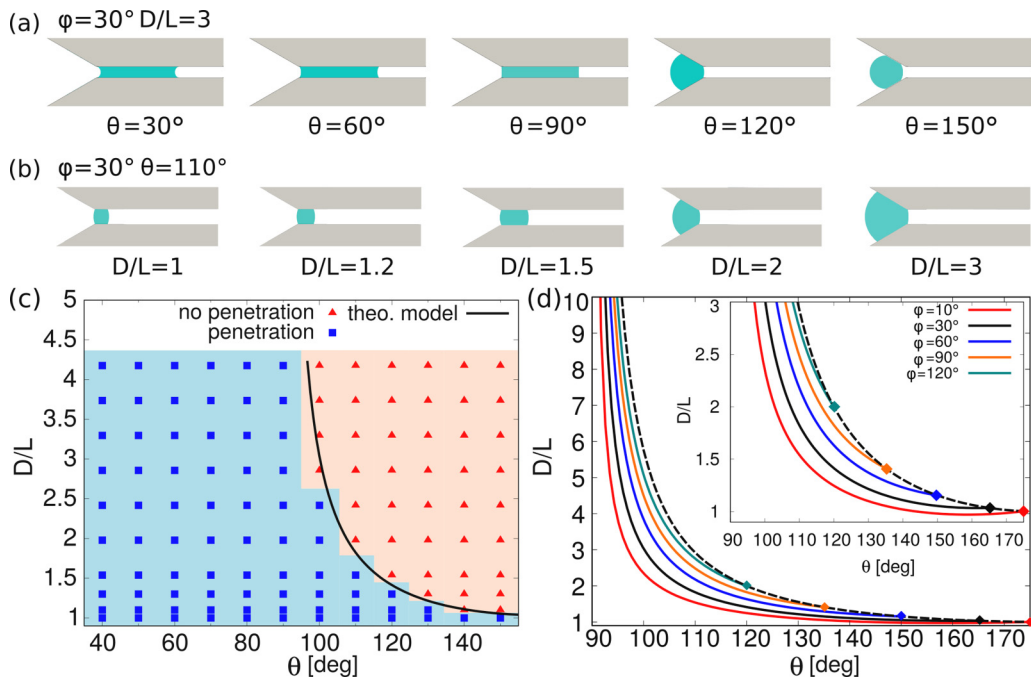
FIG. 5. Regime diagram for the end-state of droplets in funnel-like structures with different $D/L$ and $\theta$. The opening angle ($\varphi = 30°$) is constant in (a)–(c). (a),(b) The final droplet states influenced by $\theta$ and $D/L$, respectively. In (c), the blue squares and the red triangles indicate a complete penetration and no penetration, respectively. The solid curve describes the penetration critical line from the theoretical model. In (d), different colored curves show the results from the theoretical model with $\varphi$ varying from $10°$ to $120°$. The inset displays a magnification of the diagram. The black dashed curve [Eq. (12)] intersects the colored curves with different points that are highlighted by rhombus points.

critical lines become more and more steep with an enlargement of the droplet size, which reveals that the changes in the opening angle have a more profound impact on smaller droplets. It is to be expected that when $D/L \gg 1$, the curvature is not largely affected by the opening angle anymore. In this case, the critical contact angle asymptotically approaches $90°$. This is consistent with the classic conclusion in the literature that a large droplet cannot spontaneously penetrate into a hydrophobic capillary tube. It should be noted that the critical line of droplet penetration for $D/L = 1$ still exists, under which the droplet cannot completely penetrate into the channel. For instance, when $\phi = 10°$, the droplet with $D/L = 1$ at $\theta = 160°$ cannot completely penetrate. In this case, the droplet forms a liquid bridge with an aspect ratio (width/height) smaller than 1. It is highly possible that the small droplet may touch only one side of the wall and finally obtains the shape of a spherical cap. Our model is not valid for this situation anymore. Our current study mainly focuses on the situation of $D/L > 1$, thus the situation of tiny droplets with $D/L < 1$ is neglected. In Figs. 5(a)–5(c), we keep the opening angle constant ($\varphi = 30°$) and study the combined influence of the droplet size and the contact angle on the droplet penetration. Figures 5(a) and 5(b) illustrate the 2D simulation snapshots of the final droplet states by varying the contact angle and the droplet size, respectively. As shown in Fig. 5(a) for $\varphi = 30°$ and $D/L = 3$, the droplet completely penetrates into a hydrophilic channel ($\theta = 30°$, $60°$, and $90°$), whereas this is not possible for a hydrophobic substrate with $\theta = 120°$ and $150°$. For a hydrophobic substrate ($\theta = 110°$), the droplet moves into the channel when the droplet is sufficiently small, as demonstrated in the first three panels in Fig. 5(b). These states can be obtained because we initially release the circled droplets inside the left wedge, and the inner wall is tangential to the droplet profile [see, e.g., Figs. 1(a) or 1(b), the first snapshot]. It is also possible
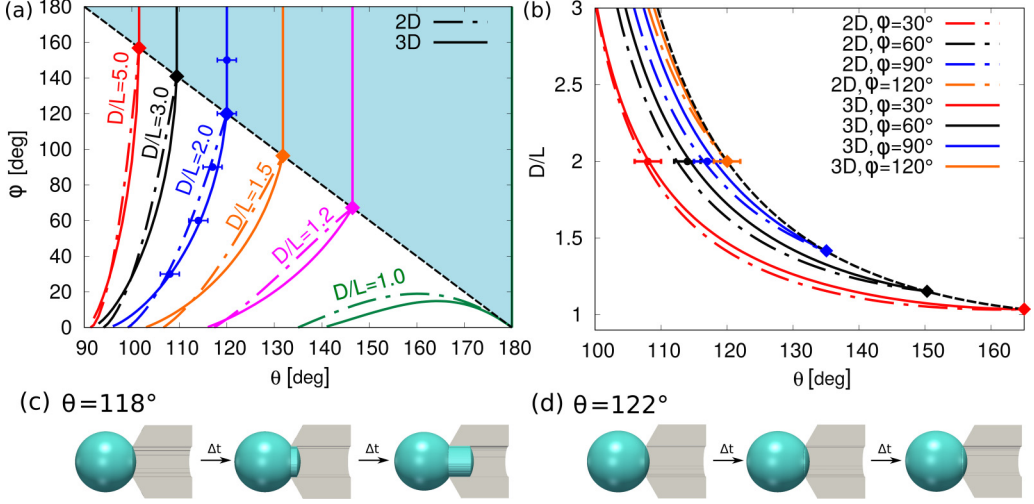
FIG. 6. Comparison of 2D and 3D theoretical predictions for the penetration critical lines. (a) The penetration critical lines as a function of $\varphi$ and $\theta$. (b) The penetration critical lines as a function of $D/L$ and $\theta$. The penetration critical lines via the 2D model (dot-dashed line) and the 3D model (solid line) for different values of $D/L$ in (a) [or $\varphi$ in (b)] are displayed in different colors. The black dashed line in (a) is described by Eq. (12). The black dashed curve in (b) shows model 1 [Eq. (9)]. The colored circle points with scattering bars are results of the binary search algorithm via 3D simulations. Parts (c) and (d) show 3D simulations for $\theta = 118°$ and $122°$, respectively. For both cases, $\varphi = 120°$ and $D/L = 2$.

that small droplets may touch only one side of the wall and stay on the flat wall. So both cases are stable states but they are dependent on the initial states of the droplets, but our model only addresses the former case. With an increase in the droplet size, a complete penetration cannot be achieved, as depicted by the last two panels in Fig. 5(b). The penetration states from the 2D simulation results are displayed in Fig. 5(c) for $D/L \in [1, 4.2]$ and $\theta \in [40°, 150°]$. The theoretical prediction of the penetration critical line is represented by the solid line, which shows a very good agreement with the simulation results. As described by the penetration state map, a low volume droplet with a small contact angle is more prone to penetrate into the channel of the funnel structure. In the hydrophilic region ($\theta \leqslant 90°$), penetration is inevitable irrespective of the droplet volume.

Figure 5(d) presents the 2D theoretical predictions via model 1 (black dashed line, $\theta \in [\theta_t, 180°)$) and model 2 (colored lines, $\theta \in (90°, \theta_t]$) for a series of opening angles. The intersections $[\theta_t, (D/L)_t]$ of models 1 and 2 are highlighted by colored rhombus points. The subscript $t$ indicates the boundary state, and $[\theta_t, (D/L)_t]$ meets with both Eqs. (9) and (10). All the penetration critical lines show the same tendency that the critical contact angle increases with a decrease in the droplet size but in two stages: (i) decreasing along the colored line in the range of $\varphi \in (90°, \theta_t]$; and (ii) decreasing along the black dashed line in the range of $\theta \in [\theta_t, 180°]$. Moreover, it is observed that a small droplet is more sensitive to the change in the opening angle, while a large droplet is more robust to the influence of the opening angle. All the penetration critical lines asymptotically approach $90°$ as the droplet becomes extremely large.

The above discussions are based on 2D analysis. Here, we further consider the 3D conical structures, which are obtained by rotating the 2D geometries along the axis of symmetry. Figures 6(a) and 6(b) present a comparison of 2D [dot-dashed lines, Eq. (10)] and 3D [solid lines, Eq. (11)] theoretical predictions of the penetration critical lines. The circle points with scattering bars via a binary search algorithm indicate the 3D simulation results for the critical states, which confirms the 3D theoretical model for $D/L = 2$. As shown in Figs. 6(c) and 6(d), the 3D droplet penetrates into the channel for $\theta = 118°$ but stays outside of the channel for $\theta = 122°$. To avoid

repeated confirmations of a similar situation for other droplet sizes, additional 3D simulations are not performed anymore. It is found that there is only a slight difference between the 2D and 3D theoretical models in the situation in which model 2 is valid. Note that model 1 in 3D is exactly the same as in the 2D case. This implies that the conclusions for the 2D situation also work for the 3D scenario.

## VI. CONCLUSIONS

The droplet penetration behavior into a 2D funnel-shaped structure has been investigated for a wide range of droplet sizes, contact angles, and opening angles. Based on the geometric analysis of droplet shapes and the pore structures, we proposed two theoretical models to address the regime maps of penetration and no penetration, which are confirmed by the comprehensive phase-field simulations. It is found that for a fixed droplet size $D/L$, the critical contact angle increases with the opening angle until a certain value of the opening angle $2\varphi_t$ is achieved. Above the opening angle $2\varphi_t$, the critical contact angle is not affected by the opening angle anymore. Furthermore, for a certain opening angle, the critical contact angle increases upon decreasing the droplet size, and a relatively small droplet is more sensitive to the influence of the opening angle. Additionally, we considered the 3D conical structures by rotating the 2D geometries along the axis of symmetry, and only a tiny difference exists between 2D and 3D predictions, thus similar findings were observed in the 3D scenario. It is noteworthy that the equilibrated droplet in a hydrophobic wedge with a certain range of different opening angles tends to be a truncated sphere (in 3D) or a truncated circle (in 2D), as discussed in Ref. [12] and Fig. 2. However, the equilibrium shape of the droplet in a funnel-like structure is highly dependent on the opening angle. Only when the opening angle is larger than a certain threshold does the equilibrium shape of the droplet become a sphere (in 3D) or a circle (in 2D).

As previously demonstrated by Marmur [6], a complete penetration into a capillary can be achieved for contact angles up to about $114°$ for sufficiently small droplets, but this conclusion is based on a straight tube. In the current work, by changing the opening angle of the funnel-like structure together with the droplet size, we have extended this contact angle limit for the complete penetration of droplets. To sum up, our findings demonstrate that the droplet penetration behavior can be accurately controlled through the droplet volume, the opening angle, and the wettability of the pore structure. The thorough study of the combined influence of these three factors to the droplet penetration paves a way to better understand wetting behaviors in a pore structure. As a future perspective, appropriate modifications to our current model would permit the study of deformable substrates, leading to a smart way of directional transport of droplets. Our endeavors in this direction may provide essential guidelines for practical applications including microfluidics, filter systems, drainage systems, oil recovery systems, and so on.

## ACKNOWLEDGMENTS

## APPENDIX A: SETUPS OF CONTACT ANGLES IN HYDROPHOBIC REGION

Table I lists the setups of different contact angles via the interfacial energy parameters $\gamma_{gs}$ and $\gamma_{ls}$, which appear in the wall free-energy density in Eq. (2). The contact angles are calculated through $\cos\theta = (\gamma_{gs}^* - \gamma_{ls}^*)/\gamma_{lg}$, with $\gamma_{gs}^* = f_w(\phi_{s0}) + \int_0^{\phi_{s0}} 2\sqrt{\gamma_{lg}w(\phi)}d\phi$ and $\gamma_{ls}^* = f_w(\phi_{s1}) + \int_{\phi_{s1}}^1 2\sqrt{\gamma_{lg}w(\phi)}d\phi$. The surface compositions from theory $(\phi_{s0}, \phi_{s1})_{\text{theor}}$ and from simulation

TABLE I. Setups of interfacial energies and the resulting surface compositions for different contact angles.

| $\theta$ | $(\gamma_{gs}, \gamma_{ls})$ | $(\gamma_{gs}^*, \gamma_{ls}^*)$ | $(\phi_{s0}, \phi_{s1})_{\text{theor}}$ | $(\phi_{s0}, \phi_{s1})_{\text{sim}}$ |
|---|---|---|---|---|
| 100° | (1, 1.174) | (1, 1.174) | (0, 1) | (0, 1) |
| 110° | (1, 1.342) | (1, 1.342) | (0, 1) | (0, 1) |
| 120° | (1, 1.500) | (1, 1.500) | (0, 1) | (0, 1) |
| 132° | (1, 1.669) | (1, 1.669) | (0, 1) | (0, 1) |
| 148° | (1, 1.700) | (1, 1.848) | (0, 0.429) | (0, 0.419) |
| 161° | (1, 2.500) | (1, 1.943) | (0, 0.180) | (0, 0.176) |
| 170° | (1, 6.000) | (1, 1.985) | (0, 0.071) | (0, 0.073) |
| 178° | (1, 101.0) | (1, 1.999) | (0, 0.009) | (0, 0.011) |

$(\phi_{s0}, \phi_{s1})_{\text{sim}}$ are obtained by solving the equation $2\sqrt{\gamma_{lg}w(\phi)} = f_w'(\phi)$ via Newton's iteration method and by measuring the value in simulations, respectively. As shown in Fig. 7, when $\theta < 132.5°$, the curves $g_1(\phi) = 2\sqrt{\gamma_{lg}w(\phi)}$ and $g_2(\phi) = f_w'(\phi)$ always intersect at (0,0) and (1,0). However, when $\theta > 132.5°$, two other intersections $[\phi_{s1}, g_1(\phi_{s1})]$ and $[1 - \phi_{s1}, g_1(1 - \phi_{s1})]$ appear, relating to additional energy minimum states. According to Refs. [31–33], the left intersection $[\phi_{s1}, g_1(\phi_{s1})]$ corresponds to a hydrophobic surface, while the right solution $[1 - \phi_{s1}, g_1(1 - \phi_{s1})]$ corresponds to a hydrophilic setup. In this work, we focus on the hydrophobic setup, thus the intersection point $[1 - \phi_{s1}, g_1(1 - \phi_{s1})]$ is not considered. We have examined the equilibrium surface composition on hydrophobic substrates through phase-field simulations. It is found that when $\theta > 132.5°$, the solutions (0,0) and $[\phi_{s1}, g_1(\phi_{s1})]$ are more energetically stable. However, when $90° < \theta < 132.5°$, the intersections (0,0) and (0,1) are the only solutions (see the last column in Table I). We have validated the contact angles by analyzing the equilibrium states of a 2D droplet in a 2D wedge as illustrated in Fig. 2. The simulations show excellent agreement with the theoretical predictions.

## APPENDIX B: MODEL 2 IN 2D

Model 2 considers the critical state, for which the left and right interfaces of the droplet are not on a joint circle. As presented in Figs. 2(b) and 2(c), the blue and red dashed circles depict the
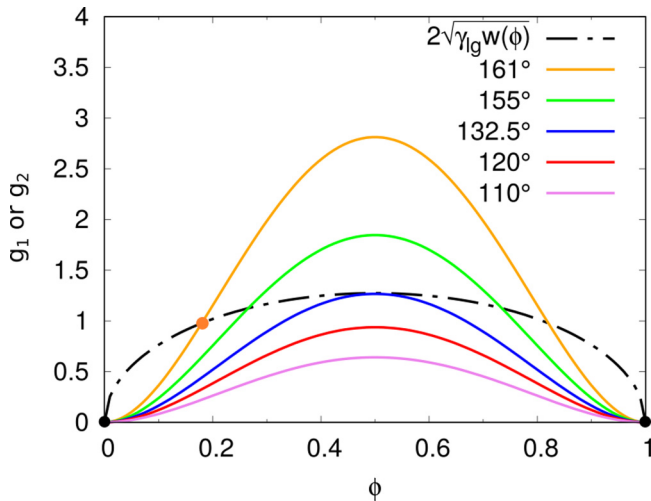


FIG. 7. The intersections between the curves $g_1(\phi) = 2\sqrt{\gamma_{lg}w(\phi)}$ (dot dashed line) and $g_2(\phi) = f_w'(\phi)$ for different contact angles (colored curves). The different contact angles are controlled via the value of $(\gamma_{gs}^* - \gamma_{ls}^*)$, which is affected by the intersection point.

left and right interfaces of the droplet, respectively. At equilibrium, these two circles have the same curvature radius $R$. The volume conservation of the droplet leads to the following equation:

$$S_{\mathrm{I}} + S_{\mathrm{II}} + S_{\mathrm{III}} = \pi D^2/4. \tag{B1}$$

Here, $S_{\mathrm{I}}$, $S_{\mathrm{II}}$, and $S_{\mathrm{III}}$ are the surface areas of the segment $M_1 M_2$ confined by the arch and chord $M_1 M_2$ corresponding to $\angle M_1 O_2 M_2$, the segment $N_1 N_2$ confined by the arch and chord $N_1 N_2$ corresponding to $\angle N_1 O_1 N_2$, and the trapezoid $M_1 M_2 N_1 N_2$, respectively. $D$ is the initial diameter of the droplet. Defining the angles $\theta_1 := \pi - \theta$ and $\theta_2 := \pi - \theta - \varphi$, we have the following expressions for $S_{\mathrm{III}}$, $S_{\mathrm{IV}}$, and $S_{\mathrm{V}}$:

$$S_{\mathrm{I}} = R^2(\pi/2 - \theta_1 - \sin\theta_1 \cos\theta_1),$$
$$S_{\mathrm{II}} = R^2(\pi/2 - \theta_2 - \sin\theta_2 \cos\theta_2),$$
$$S_{\mathrm{III}} = 0.5(L + 2R\cos\theta_2)H.$$

Here, $H = (R\cos\theta_2 - 0.5L)\cot\varphi$ is the height of the trapezoid $M_1 M_2 N_1 N_2$. In the case of $0 < \varphi < \pi/2$ [Fig. 2(b)], $\pi/2 < \varphi < \pi$ [Fig. 2(c)], and $\varphi = \pi/2$, the height $H$ and the surface area $S_{\mathrm{III}}$ are positive, negative, and zero, respectively. Substituting the expressions for $S_{\mathrm{I}}$, $S_{\mathrm{II}}$, and $S_{\mathrm{III}}$ into Eq. (B1), we obtain the model 2 in 2D [see Eq. (10)].

### APPENDIX C: MODEL 2 IN 3D

In the 3D situation, the volume conservation of the droplet leads to the following equation:

$$V_{\mathrm{IV}} + V_{\mathrm{V}} + V_{\mathrm{VI}} = \pi D^3/6. \tag{C1}$$

Here, $V_{\mathrm{IV}}$, $V_{\mathrm{V}}$, and $V_{\mathrm{VI}}$ are the volumes of the geometries formed by rotating the segment $M_1 M_2$ confined by the arch and chord $M_1 M_2$ corresponding to $\angle M_1 O_2 M_2$, the segment $N_1 N_2$ confined by the arch and chord $N_1 N_2$ corresponding to $\angle N_1 O_1 N_2$, and the trapezoid $M_1 M_2 N_1 N_2$ along the dot-dashed center line, respectively. $D$ is the initial diameter of the droplet. Defining the angles $\theta_1 := \pi - \theta$ and $\theta_2 := \pi - \theta - \varphi$, we have the following expressions for $V_{\mathrm{III}}$, $V_{\mathrm{IV}}$, and $V_{\mathrm{V}}$:

$$V_{\mathrm{IV}} = (\pi R^3/3)(2 + \sin\theta_1)(1 - \sin\theta_1)^2,$$
$$V_{\mathrm{V}} = (\pi R^3/3)(2 + \sin\theta_2)(1 - \sin\theta_2)^2,$$
$$V_{\mathrm{VI}} = (\pi R^3/3)(\cos^3\theta_2 - \cos^3\theta_1)/\tan\varphi.$$

In the case of $0 < \varphi < \pi/2$, $\pi/2 < \varphi < \pi$, and $\varphi = \pi/2$, the volume $V_{\mathrm{VI}}$ is positive, negative, and zero, respectively. Substituting the expressions for $V_{\mathrm{IV}}$, $V_{\mathrm{V}}$, and $V_{\mathrm{VI}}$ into Eq. (C1), we obtain model 2 in 3D [Eq. (11)].

Model 2 (both in 2D and 3D) is valid for $0 < \varphi \leqslant \varphi_t$, where $\varphi_t$ meets with Eq. (12).

### APPENDIX D: SPECIAL CASES FOR $\varphi = 0$

The above calculation in model 2 does not consider the case $\varphi = 0$. When the opening angle is zero, we obtain the classic straight capillary tube, where the droplet forms a symmetric liquid bridge. In this case, the height $H$ is independent of the opening angle $2\varphi$. When $H = L\tan(\pi - \theta)$ [see Fig. 8(b)], we obtain the relationship in 2D,

$$\frac{D}{L} = \sqrt{\frac{2\theta - \sin 2\theta - \pi}{\pi \cos^2\theta}}. \tag{D1}$$

In 3D (cylinder tube), the relationship becomes

$$\frac{D}{L} = \sqrt[3]{\frac{(2 + \sin\theta)(1 - \sin\theta)^2 + 3\sin\theta\cos^2\theta}{2\cos(\pi - \theta)}}. \tag{D2}$$
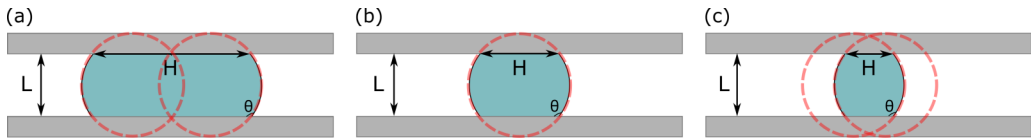
FIG. 8. When $\varphi = 0$, the funnel-like structure becomes a classic straight capillary tube, where the droplet forms a symmetric liquid bridge. (a) $H > L\tan(\pi - \theta)$. (b) $H = L\tan(\pi - \theta)$. (c) $H < L\tan(\pi - \theta)$. The red dashed line is a circular fit of the droplet interface.

The above equations are valid for $\theta > 90°$. In particular, when $\theta = 180°$, we obtain $D/L = 1$, which corresponds to the situation in which the 2D circular droplet or the 3D spherical droplet is tangent to the inner wall of the capillary tube. The calculation $H = L\tan(\pi - \theta)$ is based on the assumption that the left and right interfaces of the droplet are on a joint circle. The circumstances in which the interfaces of the droplet are not on a common circle, i.e., $H > L\tan(\pi - \theta)$ (large droplet) and $H < L\tan(\pi - \theta)$ (small droplet), are indicated in Figs. 8(a) and 8(c), respectively. For more details of a liquid bridge on different structures, we refer the reader to Refs. [1,41,42].

[1] D. Langbein, Liquid penetration into tubes and wedges, in *Capillary Surfaces* (Springer, Berlin, Heidelberg, 2002) pp. 259–285.

[2] R. Finn, *Equilibrium Capillary Surfaces* (Springer Science & Business Media, New York, 2012), Vol. 284.

[3] R. Lucas, Ueber das zeitgesetz des kapillaren aufstiegs von flüssigkeiten, Kolloid Z. **23**, 15 (1918).

[4] E. W. Washburn, The dynamics of capillary flow, Phys. Rev. **17**, 273 (1921).

[5] D. Bonn, J. Eggers, J. Indekeu, J. Meunier, and E. Rolley, Wetting and spreading, Rev. Mod. Phys. **81**, 739 (2009).

[6] A. Marmur, Penetration of a small drop into a capillary, J. Colloid Interface Sci. **122**, 209 (1988).

[7] G. R. Willmott, C. Neto, and S. C. Hendy, Uptake of water droplets by non-wetting capillaries, Soft Matter **7**, 2357 (2011).

[8] T. Andrukh, D. Monaenkova, B. Rubin, W.-K. Lee, and K. G. Kornev, Meniscus formation in a capillary and the role of contact line friction, Soft Matter **10**, 609 (2014).

[9] P. Yue and Y. Renardy, Spontaneous penetration of a non-wetting drop into an exposed pore, Phys. Fluids **25**, 052104 (2013).

[10] E. H. Hauge, Macroscopic theory of wetting in a wedge, Phys. Rev. A **46**, 4994 (1992).

[11] K. Rejmer, S. Dietrich, and M. Napiórkowski, Filling transition for a wedge, Phys. Rev. E **60**, 4027 (1999).

[12] D. Baratian, A. Cavalli, D. Van Den Ende, and F. Mugele, On the shape of a droplet in a wedge: New insight from electrowetting, Soft Matter **11**, 7717 (2015).

[13] É. Ruiz-Gutiérrez, C. Semprebon, G. McHale, and R. Ledesma-Aguilar, Statics and dynamics of liquid barrels in wedge geometries, J. Fluid Mech. **842**, 26 (2018).

[14] G. Kubalski and M. Napiórkowski, A liquid drop in a cone-line tension effect, J. Phys.: Condens. Matter **12**, 9221 (2000).

[15] S. M. McFaul, B. K. Lin, and H. Ma, Cell separation based on size and deformability using microfluidic funnel ratchets, Lab Chip **12**, 2369 (2012).

[16] E. Benet and F. J. Vernerey, Mechanics and stability of vesicles and droplets in confined spaces, Phys. Rev. E **94**, 062613 (2016).

[17] M. Zimmermann, P. Hunziker, and E. Delamarche, Valves for autonomous capillary systems, Microfluid. Nanofluid. **5**, 395 (2008).

[18] Y. Kaufman, S.-Y. Chen, H. Mishra, A. M. Schrader, D. W. Lee, S. Das, S. H. Donaldson Jr., and J. N. Israelachvili, Simple-to-apply wetting model to predict thermodynamically stable and metastable contact angles on textured/rough/patterned surfaces, J. Phys. Chem. C **121**, 5642 (2017).

[19] J. Li, X. Zhou, J. Li, L. Che, J. Yao, G. McHale, M. K. Chaudhury, and Z. Wang, Topological liquid diode, Sci. Adv. **3**, eaao3530 (2017).

[20] M. Prakash, D. Quéré, and J. W. Bush, Surface tension transport of prey by feeding shorebirds: The capillary ratchet, Science **320**, 931 (2008).

[21] W. Kim and J. W. Bush, Natural drinking strategies, J. Fluid Mech. **705**, 7 (2012).

[22] B. Dai, K. Li, L. Shi, X. Wan, X. Liu, F. Zhang, L. Jiang, and S. Wang, Bioinspired janus textile with conical micropores for human body moisture and thermal management, Adv. Mater. **31**, 1904113 (2019).

[23] B. Nestler, F. Wendler, M. Selzer, B. Stinner, and H. Garcke, Phase-field model for multiphase systems with preserved volume fractions, Phys. Rev. E **78**, 011604 (2008).

[24] H. Kusumaatmaja, J. Leopoldes, A. Dupuis, and J. Yeomans, Drop dynamics on chemically patterned surfaces, Europhys. Lett. **73**, 740 (2006).

[25] M. Ben Said, M. Selzer, B. Nestler, D. Braun, C. Greiner, and H. Garcke, A phase-field approach for wetting phenomena of multiphase droplets on solid surfaces, Langmuir **30**, 4033 (2014).

[26] A. Badillo, Quantitative phase-field modeling for wetting phenomena, Phys. Rev. E **91**, 033005 (2015).

[27] Y. Wu, F. Wang, M. Selzer, and B. Nestler, Droplets on chemically patterned surface: A local free-energy minima analysis, Phys. Rev. E **100**, 041102(R) (2019).

[28] V. Khatavkar, P. Anderson, and H. Meijer, Capillary spreading of a droplet in the partially wetting regime using a diffuse-interface model, J. Fluid Mech. **572**, 367 (2007).

[29] D. Jacqmin, Calculation of two-phase navier-stokes flows using phase-field modeling, J. Comput. Phys. **155**, 96 (1999).

[30] X. Xu and X. Wang, Derivation of the wenzel and cassie equations from a phase field model for two phase flow on rough surface, SIAM J. Appl. Math. **70**, 2929 (2010).

[31] J. W. Cahn, Critical point wetting, J. Chem. Phys. **66**, 3667 (1977).

[32] P.-G. De Gennes, Wetting: Statics and dynamics, Rev. Mod. Phys. **57**, 827 (1985).

[33] F. Wang and B. Nestler, Wetting transition and phase separation on flat substrates and in porous structures, J. Chem. Phys. **154**, 094704 (2021).

[34] Y. Wu, F. Wang, M. Selzer, and B. Nestler, Investigation of equilibrium droplet shapes on chemically striped patterned surfaces using phase-field method, Langmuir **35**, 8500 (2019).

[35] Y. Wu, M. Kuzina, F. Wang, M. Reischl, M. Selzer, B. Nestler, and P. A. Levkin, Equilibrium droplet shapes on chemically patterned surfaces: theoretical calculation, phase-field simulation, and experiments, J. Colloid Interface Sci. **606**, 1077 (2022).

[36] D.-H. Choi, G.-W. Yoon, J. W. Park, C. Ihm, D.-S. Lee, and J.-B. Yoon, Fabrication of a membrane filter with controlled pore shape and its application to cell separation and strong single cell trapping, J. Micromech. Microeng. **25**, 105007 (2015).

[37] R. Hensel, K. Moh, and E. Arzt, Engineering micropatterned dry adhesives: from contact theory to handling applications, Adv. Funct. Mater. **28**, 1800865 (2018).

[38] J. R. Panter, Y. Gizaw, and H. Kusumaatmaja, Critical pressure asymmetry in the enclosed fluid diode, Langmuir **36**, 7463 (2020).

[39] P. Concus and R. Finn, On the behavior of a capillary surface in a wedge, Proc. Natl. Acad. Sci. (USA) **63**, 292 (1969).

[40] C. Huh and L. E. Scriven, Hydrodynamic model of steady movement of a solid/liquid/fluid contact line, J. Colloid Interface Sci. **35**, 85 (1971).

[41] B. J. Lowry and P. H. Steen, Capillary surfaces: stability from families of equilibria with application to the liquid bridge, Proc. R. Soc. London, Ser. A **449**, 411 (1995).

[42] J. Bostwick and P. Steen, Stability of constrained capillary surfaces, Annu. Rev. Fluid Mech. **47**, 539 (2015).

*Correction:* The previously published Figure 6 contained errors in the images in panels (c) and (d) and has been replaced.